crystals

MDPI

Essay

Effect of Solution Annealing Time on the Microstructure and Mechanical Properties of Selective-Laser-Melted 2205 Duplex Stainless Steel

Huanhuan Li, Jinyuan Ma, Guang Li, Wenzhu Zhang, Xianheng Bao and Yu Shi *

State Key Laboratory of Advanced Processing and Recycling of Non-Ferrous Metals, Lanzhou University of Technology, Lanzhou 730050, China
* Correspondence: shiyu@lut.edu.cn

Abstract: The 2205 duplex stainless steel (DSS) produced by selective laser melting (SLM) exhibits high strength (1078.8 MPa) but poor plasticity (15.2%) owing to the high cooling rate during SLM, which inhibits the formation of austenite and creates a nearly entirely ferritic microstructure. The dual-phase nature can be restored through solution annealing, which enables well-matched strength and plasticity, but which has not been extensively studied. We investigate the effects of 5 min, 30 min, and 120 min of solution annealing at 1000 °C on the dual-phase ratio, grain size, texture strength, inclusions, grain boundary characteristics, and mechanical properties of SLM-manufactured 2205 DSS. After 30 min of solution annealing, the elongation increased to 32.2% owing to the restoration of the dual-phase structure, the reduction in dislocation density, the weakening of texture, and the decrease in grain size. Increasing solution annealing time also corresponded to a decrease in the ultimate tensile strength (from 831.7 to 787.5 MPa) and yield strength (from 610.3 to 507.8 MPa) due to grain coarsening and the gradual transformation of ferrite to austenite. Furthermore, the mechanism of the transformation from ferrite to austenite was proposed, and it was observed that the transformation of $MnSiO_3$ to $MnCrO_4$ provided nucleation sites for austenite.

Keywords: selective laser melting; duplex stainless steel; solution annealing time; microstructure; mechanical properties

check for updates

Citation: Li, H.; Ma, J.; Li, G.; Zhang, W.; Bao, X.; Shi, Y. Effect of Solution Annealing Time on the Microstructure and Mechanical Properties of Selective-Laser-Melted 2205 Duplex Stainless Steel. *Crystals* **2024**, *14*, 229. https://doi.org/10.3390/cryst14030229

Academic Editor: Marek Sroka

Received: 25 January 2024
Revised: 21 February 2024
Accepted: 26 February 2024
Published: 28 February 2024

1. Introduction

Duplex stainless steel (DSS) has a dual-phase microstructure, consisting of ferrite and austenite, that provides a high strength, good ductility, and excellent corrosion resistance [1]. DSS is therefore widely used in the papermaking and petrochemical industries, particularly for devices such as chemical tankers and pressure vessels [2,3]. However, austenite and ferrite exhibit different strain-hardening behaviors, resulting in phase inhomogeneity and mismatch. This makes DSS prone to cracking during hot processing and limits its application to complex components [4]. Additionally, the performance of DSS is significantly influenced by the ratios of ferrite and austenite, which are largely determined by factors such as the chemical composition of the steel and the solution annealing regime. Therefore, appropriate solution annealing methods are particularly important for the application of DSS.

Compared to traditional manufacturing processes, selective laser melting (SLM) can directly produce high-precision complex parts while maintaining excellent mechanical properties [5–7]. Therefore, SLM has been widely applied to titanium alloys [8,9], aluminum alloys [10,11], copper alloys [12,13], nickel-based superalloys [14–16], and other metals [17,18]. Research on the SLM of stainless steel mainly focuses on austenitic stainless steel [19–21] and precipitation-hardened stainless steel [22–24], while research regarding the SLM of DSS is less common.

Some research indicates that, unlike the excellent mechanical properties of other SLM-manufactured alloys, the microstructure of DSS manufactured by SLM is primarily ferritic (>95%), resulting in a high strength but poor elongation [3]. For example, the tensile strength of SLM-manufactured 2205 DSS can reach 872 MPa, while the elongation is only 11% [25]. Similarly, the tensile strength of alloy 2507 is 1320 MPa, with a small elongation of 8% [26]. This significantly limits the application of SLM in DSS manufacturing. Previous studies have shown that it is difficult to achieve the desired dual-phase ratio by simply adjusting the processing conditions. Post-welding or post-additive manufacturing solution annealing can alter the microstructure to improve performance [27,28]. Therefore, solution annealing presents an avenue to restore the dual-phase ratio while reducing the effects of the residual stress and dislocation generation. Table 1 summarizes the changes in the phase ratio of SLM-manufactured 2205 DSS before and after solution annealing. It can be observed that solution annealing of the as-built state can increase the content of austenite, but the degree of phase transformation depends on the heat treatment conditions. Solution annealing of the as-built state follows, with the intention of increasing the amount of austenite in the microstructure.

Hengsbach et al. [29] found that increasing the solution temperature initially led to an increase in austenite content, followed by a decrease at higher temperatures. The decrease in the austenitic phase is attributed to the loss of nitrogen at high temperatures. Among these results, the highest content of austenite exhibited the most superior mechanical properties. Xiang et al. [4] investigated the influence of solution temperature on the grain size, lattice defects, and residual stress of 2205 DSS. They found that, after solution annealing, the dual-phase microstructure is restored, with a refined grain size, reduced residual stress, and an increased occurrence of low-energy coincidence site lattice (CSL) boundaries, exhibiting outstanding strength–plasticity matching. With an increase in the solution temperature, the material strength decreased, while the strain rate remained relatively constant. As shown in Table 1, at the same temperature, the solution annealing time influences the transformation from the ferritic to the austenitic phase, with the austenite content increasing as the solution annealing time increases. Similar phenomena were observed by Pan et al. [30] in cold-rolled DSS, where an increasing solution annealing time led to an increase in the extent of transformation from the ferritic to the austenitic phase, resulting in a more balanced phase content and a more uniform microstructure. However, there is a lack of comprehensive research on the impact of solution annealing time on SLM-manufactured DSS. Specifically, there are few to no studies exploring the effects of solution annealing time on the dual-phase ratio, grain size, texture strength, inclusions, and grain boundary characteristics of SLM-manufactured DSS, nor the correlation between these changes and the mechanical properties. The current study aims to address this gap.

Table 1. Summary of reported changes in the phase composition of SLM-manufactured 2205 DSS before and after solution annealing.

Phase Composition of As-Built State		**Condition**	**Phase Composition after Solution Annealing**		**Ref.**
Ferrite (%)	**Austenite (%)**		**Ferrite (%)**	**Austenite (%)**	
99.3	0.7	1100 °C, 5 min	51.7	48.3	[25]
98.0	2.0	1000 °C, 10 min	55	45	[31]
99.0	1.0	950 °C, 5 min	59.9	40.1	[32]
		1000 °C, 50 min	56.8	43.2	
		1000 °C, 60 min	53.6	46.4	
		1050 °C, 5 min	57.0	43.0	
		1050 °C, 60 min	54.6	45.4	
		1100 °C, 50 min	57.4	42.6	
99.8	0.2	1000 °C, 60 min	39.7	60.3	[4]

Table 1. *Cont.*

Phase Composition of As-Built State		Condition	Phase Composition after Solution Annealing		Ref.
Ferrite (%)	Austenite (%)		Ferrite (%)	Austenite (%)	
99.0	1.0	1100 °C, 60 min	42.4	57.6	[29]
		1200 °C, 60 min	43.4	56.6	
		900 °C, 5 min	76.0	24.0	
		950 °C, 5 min	69.0	31.0	
		1000 °C, 5 min	66.0	34.0	
		1050 °C, 5 min	73.0	27.0	
		1100 °C, 5 min	74.0	26.0	
		1150 °C, 5 min	74.0	26.0	
		1100 °C, 5 min	79.0	21.0	

In this study, 2205 DSS powder was manufactured into high-density specimens through SLM. After subjecting these specimens to different solid-solution annealing time at a temperature of 1000 °C, their phase transformation and microstructural evolution, as well as their impact on the mechanical properties of these specimens, were investigated.

2. Materials and Methods

2.1. Materials

Commercial UNS S32205 DSS powders were produced in a HERMICA 75/5VI gas atomizer and purchased from Chengdu Kotilon Alloy Corporation (Chengdu, China). The powder was mainly distributed in a spherical shape. The particle size distribution was in the range of 15–45 μm, (Figure 1). The chemical composition is listed in Table 2. The specimens (described later) were printed on a 316 stainless steel substrate using an SLM machine (AFS-M120XT, Longyuan AFS, Beijing, China) equipped with a 500 W laser (Figure 2a). The oxygen content in the build chamber was maintained below 100 ppm under argon gas protection. To obtain specimens with a density exceeding 99%, the following process parameters were used: a laser power of 150 W, a scanning speed of 700 mm/s, a scanning spacing of 0.07 mm, a layer thickness of 0.03 mm, and a 67° rotation between layers (Figure 2b). Some of the printed specimens were kept aside as the “as-built” specimens, while the remaining specimens were treated by solution annealing at 1000 °C for 5 min, 30 min, or 120 min, respectively, and labeled as HT-5, HT-30, and HT-120, respectively.

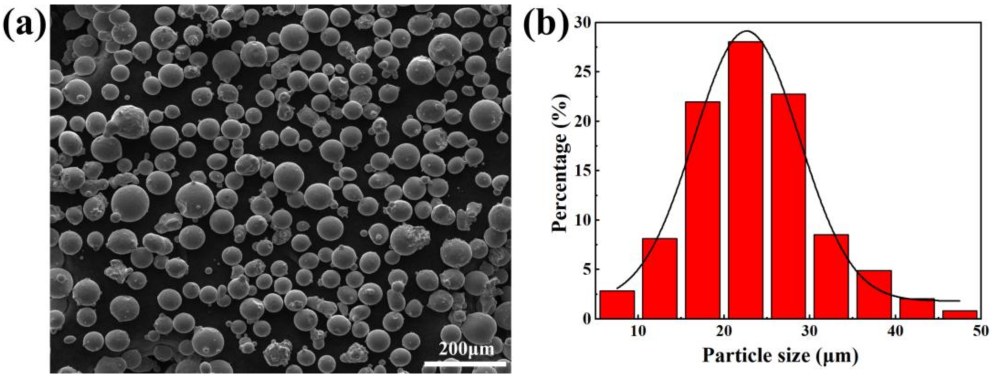

Figure 1. (**a**) SEM micrograph of 2205 DSS powders and (**b**) statistical particle size distribution.

Table 2. Chemical composition of UNS S32205 DSS powder (wt%).

C	Si	Cr	Ni	Mn	Mo	N	S	P	Fe
0.01	0.42	22.25	5.37	1.01	3.22	0.19	<0.03	<0.04	Bal.

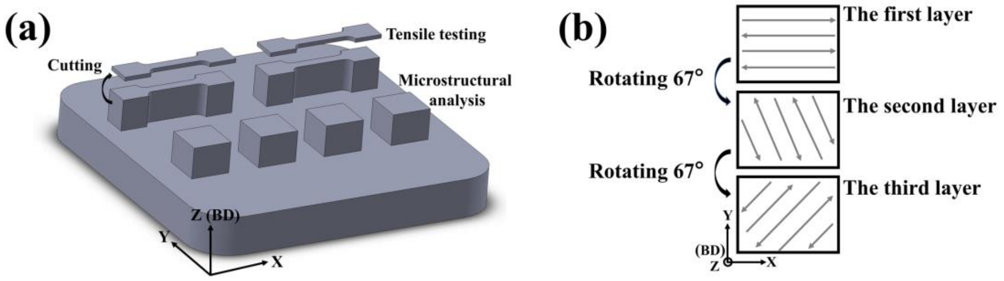

Figure 2. Tensile test specimen preparation: (**a**) distribution of specimens on stainless steel 316 substrate and (**b**) schematic of laser scanning strategy.

2.2. Microstructural Analysis

The phases of the specimens were determined using X-ray diffraction (D8-ADVANCE, Bruker, Karlsruhe, Germany) with a scanning speed of 5°/min. The fracture surfaces of the tensile specimens were examined by scanning electron microscopy (SEM) (Quanta FEG 450, FEI, Hillsboro, OR, USA). The grain size and crystallographic orientation of the specimens before and after solution annealing were investigated using electron backscatter diffraction (EBSD) employing an Oxford Instruments system. Before EBSD characterization, each sample was sequentially polished to 3000# and further electropolished for 15 s at a voltage of 20 V in a 10% alcoholic solution of high-chloric acid. The nitrogen contents of the powder and as-built specimens were measured using an NOH5000 (Focused Photonics, Hangzhou, China) instrument.

To prepare for transmission electron microscopy (TEM) analysis, the specimens were thinned down to a thickness of 50 μm and then subjected to electrolytic double-jet polishing using a 10% alcoholic solution of perchloric acid at −20 °C and 25 V. The TEM (JEOL F200, JEOL, Beijing, China) analysis was performed using bright-field imaging, energy-dispersive spectroscopy (EDS), and high-angle annular dark-field (HAADF) imaging.

2.3. Mechanical Tests

Tensile tests were conducted using an AG-X300KN (Shimadzu China, Shanghai China) tensile testing machine at a loading speed of 0.01 mm/min. Three parallel specimens were tested for each group (as-built, HT-5, HT-30, and HT-120). The average values of tensile strength and elongation until fracture were obtained. The tensile specimens were machined to a size of 12 mm × 2.5 mm × 1 mm, with a gauge length of 10 mm, according to ISO 6892-1:2009 [33]. Research by Salvetr et al. [34] suggests that there was little difference between the tensile performance of SLM-manufactured DSS perpendicular to the building direction (BD) and that parallel to the BD. Therefore, this study focuses on the tensile performance in the direction perpendicular to the building direction (Figure 2a).

3. Results

3.1. Microstructure

XRD is performed on the 2205 DSS powder specimens, before and after solution annealing. The results are shown in Figure 3. There is only a ferrite phase, with no austenite phase, in the 2205 DSS powder or the as-built specimens. Gas atomization is a technique that uses high-speed gas flow to impact a molten metal, converting the gas energy into the surface energy of the molten metal through collisions, causing it to break into fine droplets and rapidly solidify (cooling rate of 10^2–10^6 $K{\cdot}S^{-1}$) into metal particles [35]. When DSS is melted and rapidly cooled, it can result in the formation of ferrite phase due to the rapid solidification, which suppresses the formation of austenite phase in the powder [36]. The reason for the presence of only ferrite phase in the finished sample will be discussed in Section 4.2. However, as described previously, solution annealing restores the dual-phase microstructure of this material. No additional phases are detected at the different solution annealing times.

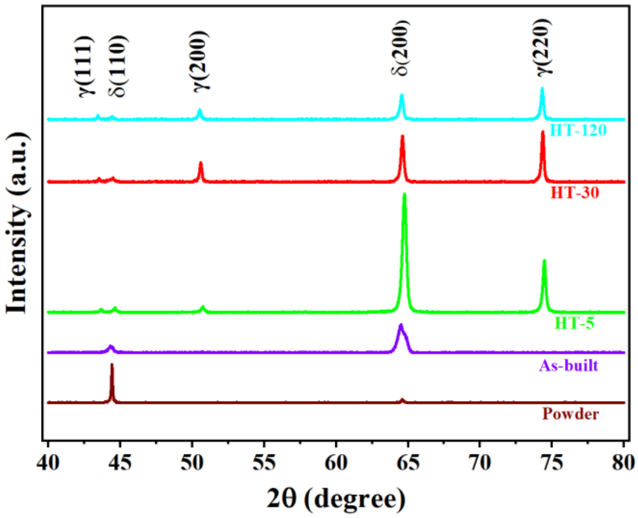

Figure 3. XRD patterns of 2205 DSS powder in specimens before and after solution annealing.

Figure 4 depicts the phase maps of the 2205 alloy specimens before and after solution annealing in the X–Y plane, where red and green indicate the ferritic and austenitic phases, respectively. The phase map for the as-built specimen (Figure 4a) is completely red, indicating an entirely ferritic microstructure. However, after solution annealing, the dual-phase structure is restored; as the solution annealing time increases, more and more austenite is formed (Figure 4b–d). The fraction of the austenite phase reaches 35 vol% after 5 min of solution annealing and achieves a maximum of 46.1 vol% after 120 min. This indicates that the ferritic and austenitic phase proportions are strongly dependent on the solution annealing time, and extending the annealing time effectively increases the fraction of the austenitic phase.

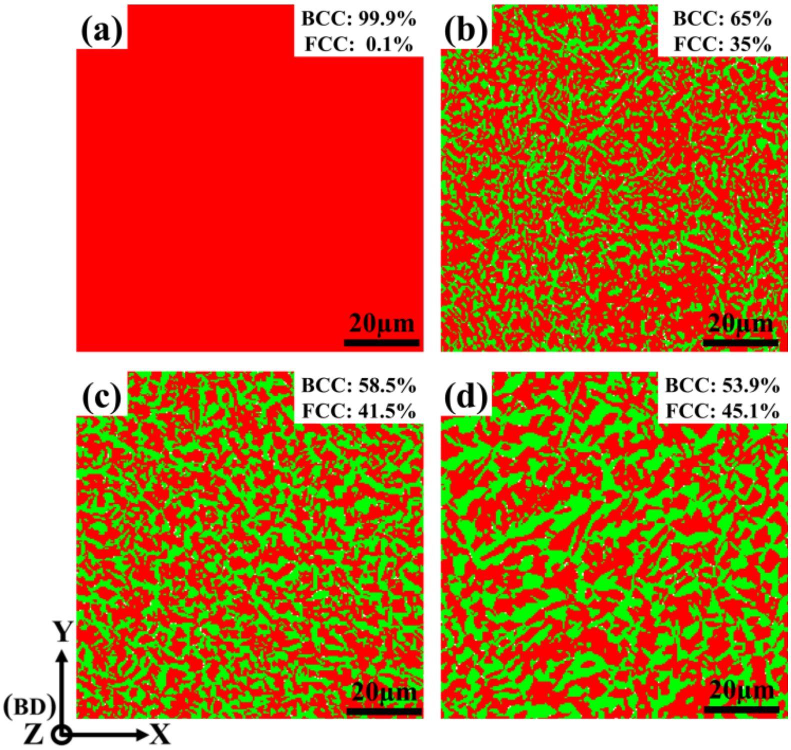

Figure 4. Phase maps, with red and green representing the ferritic and austenitic phases, respectively: (**a**) as-built, (**b**) HT-5, (**c**) HT-30, and (**d**) HT-120.

We also calculated the grain size (GS) before and after solution annealing using EBSD. The results are shown in Table 3. The as-built specimen exhibited an average grain size of 6.49 μm, which was significantly higher than that of the annealed specimens. However, the average grain size increased during annealing, from 2.29 μm in the HT-5 specimen to 2.46 μm in the HT-30 specimen, ultimately reaching 2.73 μm in the HT-120 specimen. The same trend is observed when looking at the austenite grain size in isolation. However, the ferrite grain size varied significantly, decreasing from 6.69 μm in the as-built specimen to 4.06 μm in the HT-30 specimen, before increasing again to 4.22 μm in the HT-120 specimen.

Table 3. Grain size change according to EBSD statistics.

	As-Built	**HT-5**	**HT-30**	**HT-120**
GS/μm	6.49	2.29	2.46	2.73
δ_{GS}/μm	6.69	4.29	4.06	4.22
γ_{GS}/μm	1.98	1.83	2.05	2.33

The inverse pole figure (IPF) maps (Figure 5) show the crystallographic orientations of the specimens before and after solution annealing. In the as-built specimen, the dominant orientation is the field in the <001> direction (Figure 5a). After solution annealing, the distribution of the crystallographic direction is the <001> and <101> directions (Figure 5b–d). The texture intensity of ferrite and austenite is analyzed separately (Figure 5e–h). The as-built specimen exhibits a texture intensity of 24.17 MUD, which is significantly higher than that of the annealed specimens. However, with increasing annealing time, the texture intensity of ferrite decreases from 18.99 MUD in the HT-5 specimen to 12.47 MUD in the HT-30 specimen before increasing again to 18.87 MUD in the HT-120 specimen, and the texture intensity of austenite decreases from 7.30 MUD in the HT-5 specimen to 5.61 MUD in the HT-30 specimen, before increasing again to 7.76 MUD in the HT-120 specimen. In addition, the texture intensity of ferrite is always higher than that of austenite. The ferrite exhibits a relatively strong <001>//BD texture, whereas the austenite exhibits a weak <101>//BD texture. This is similar to the results from a previous report [37].

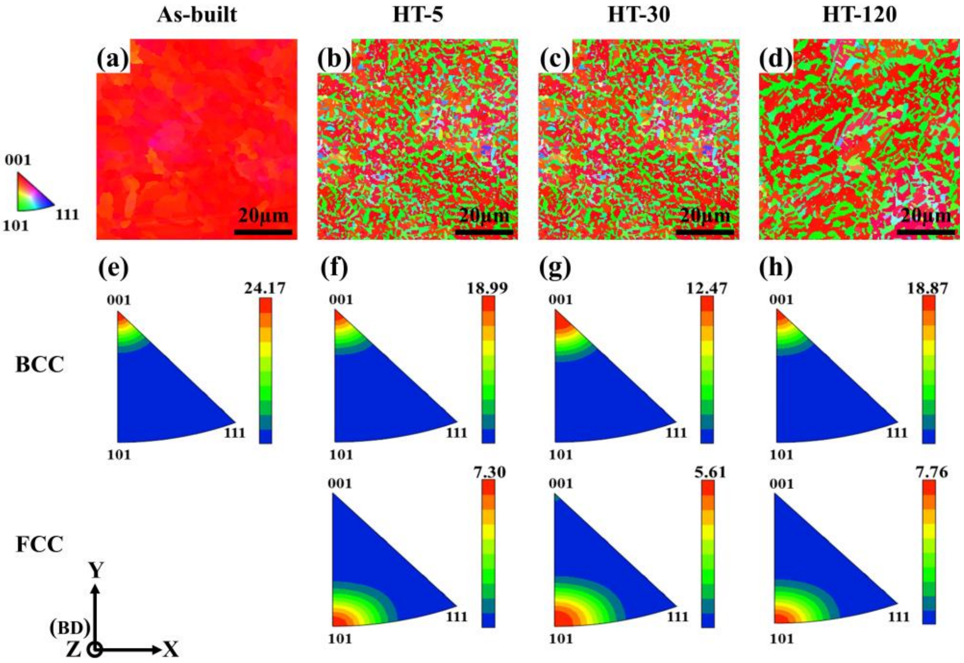

Figure 5. Inverse pole figure (IPF) maps: (**a**) as-built, (**b**) HT-5, (**c**) HT-30, and (**d**) HT-120. Texture (IPF) of ferrite and austenite: (**e**) as-built, (**f**) HT-5, (**g**) HT-30, and (**h**) HT-120.

Figure 6 displays the φ_2 = 45° sections of the ODF corresponding to the typical texture components and fibers found in ferrite and austenite [38,39]. The φ_2 = 45° sections for the two phases of the before and after solution are shown in Figure 7. Compared with the results shown in Figure 6, it is observed that the texture composition did not change before and after solid solution treatment, and the texture composition did not change with the increase in solid solution time. The ferrite exhibits a strong cube texture of {001}<001>, while the austenite exhibits a strong rotated Goss texture of {110}<110> and a Goss texture of {110}<001>.

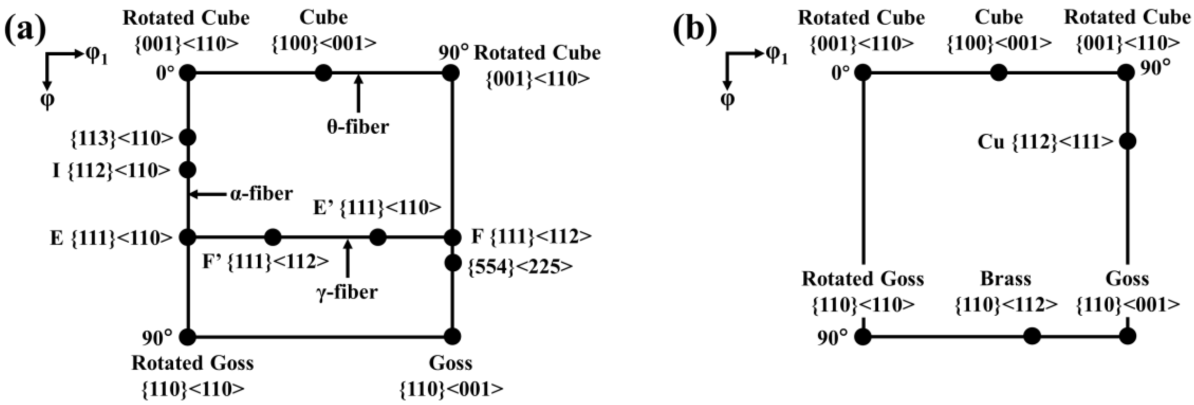

Figure 6. Typical texture components in the φ_2 = 45° section of the orientation distribution function (ODF): (**a**) BCC, and (**b**) FCC.

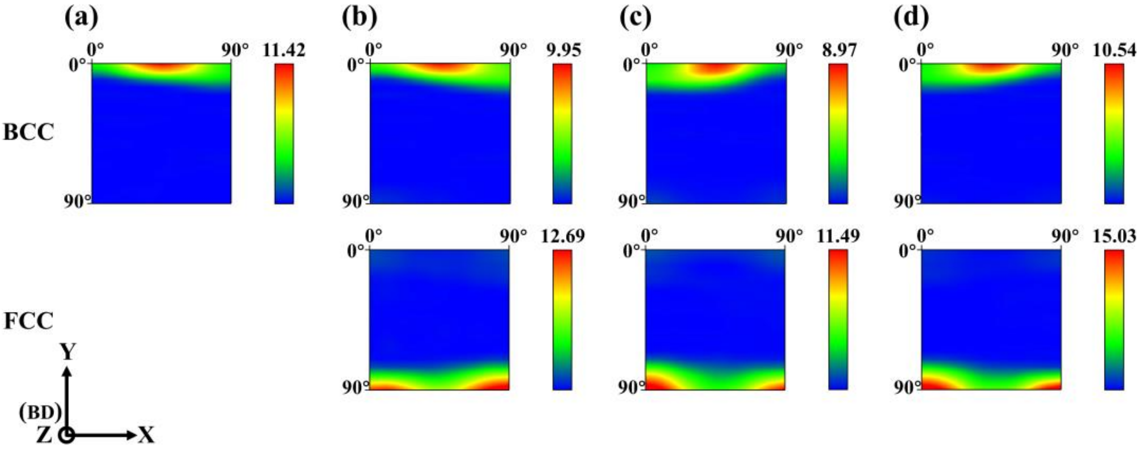

Figure 7. φ_2 = 45° section of the orientation distribution function (ODF) showing typical texture components that occur in ferrite and austenite: (**a**) as-built, (**b**) HT-5, (**c**) HT-30, and (**d**) HT-120.

Figure 8 shows the grain boundary misorientation angle distributions, before and after solution annealing. A CSL misorientation angle between adjacent grains of <15° is considered a low-angle grain boundary (LAGB), while a misorientation > 15° is considered a high-angle grain boundary (HAGB). The content of HAGB in the as-built sample is 72.43%. After solution annealing, the activation energy of dislocation climb increases, and the LAGBs are gradually consumed by subgrain boundary coalescence and migration through the cross-slip and climb of dislocations, forming the random HAGBs [4]. However, Figure 8 shows that the proportion of LAGBs increases with annealing time, from 55.5% in the HT-5 specimen to 60.5% in the HT-120 specimen. This is because the nucleation of austenite on the ferrite surface resembles sympathetic nucleation, where one grain forms at the edge or surface of another grain [37], and the boundaries of sympathetic nucleation are LAGBs [40].

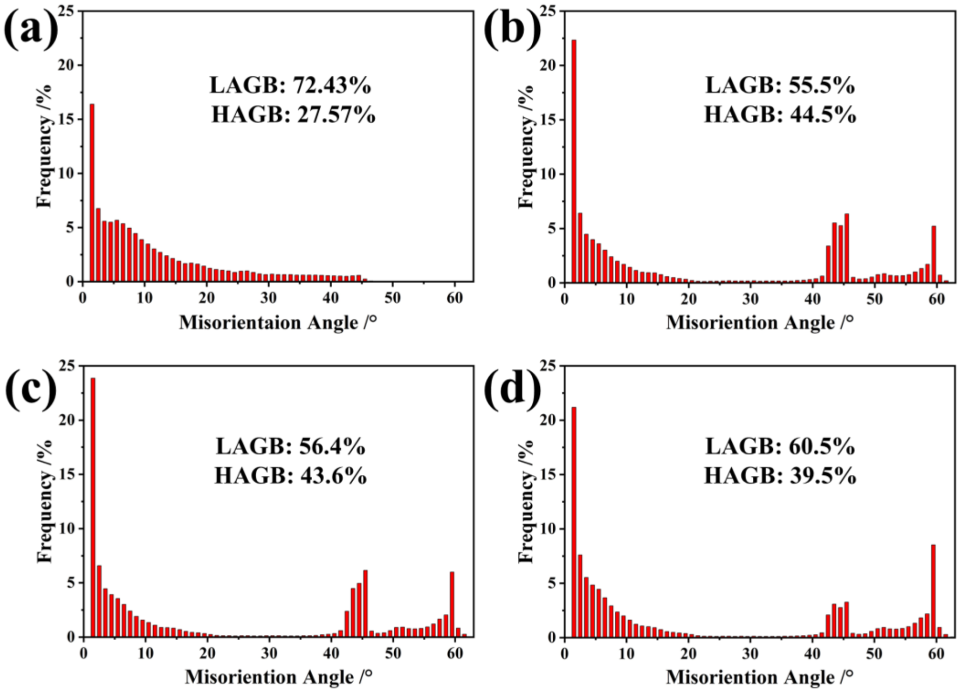

Figure 8. Grain boundary misorientation: (**a**) as-built, (**b**) HT-5, (**c**) HT-30, and (**d**) HT-120.

To identify the orientation relationship between austenite and ferrite, the phase distribution of the dual phase is determined for each specimen. The results are shown in Figure 9. After solution annealing, the ferrite {101} plane and austenite {111} plane are parallel, as are the ferrite {111} and austenite {101} planes, which follow the Kurdjumov–Sachs (K-S) orientation relationship. Similarly, the ferrite {001} plane is parallel to the austenite {101} plane, and the ferrite {101} plane is parallel to the austenite {001} plane, as per the Pitsch (P) orientation relationship.

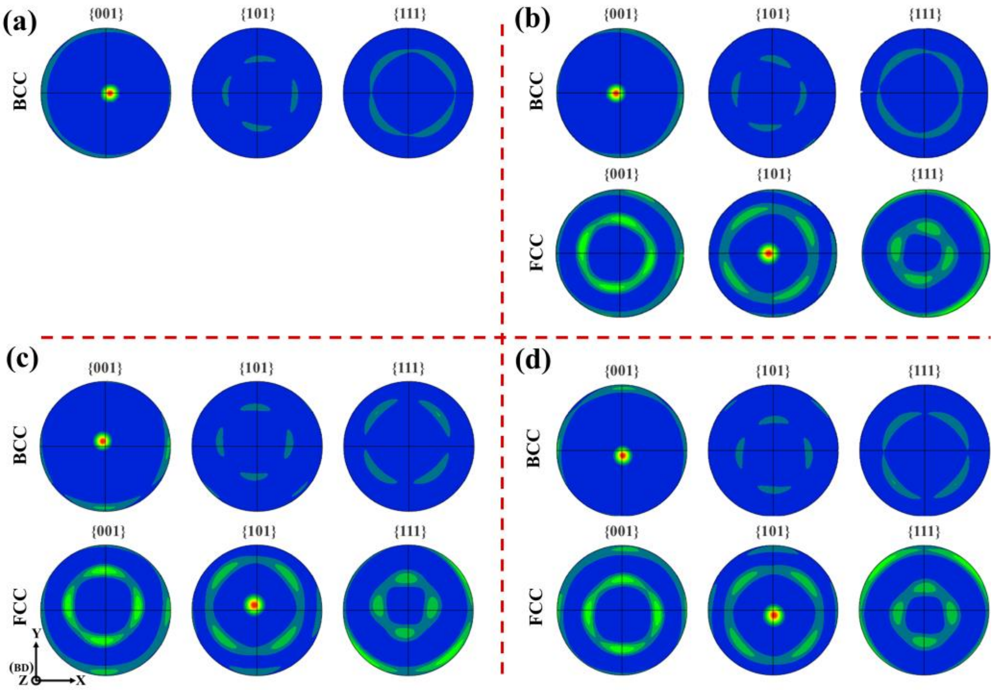

Figure 9. Pole figures of specimens: (**a**) as-built, (**b**) HT-5, (**c**) HT-30, and (**d**) HT-120.

TEM studies are conducted to analyze the structure of the specimen in detail. The TEM images reveal that the as-built specimen exhibits a high dislocation density (Figure 10a), which decreased significantly after solution annealing, as seen in the HT-30 sample (Figure 10b), owing to grain recrystallization and the motion of HAGBs [29].

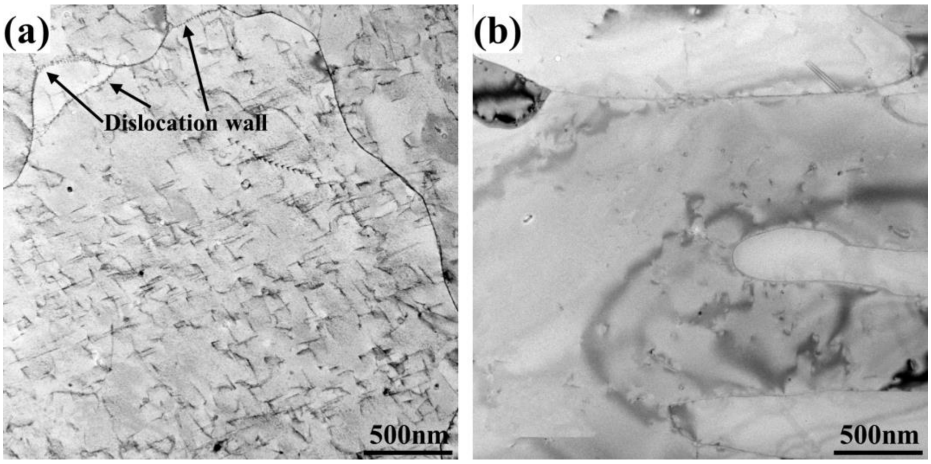

Figure 10. Bright field TEM image showing dislocations: (**a**) as-built and (**b**) HT-30.

Furthermore, numerous inclusions are observed in the specimens before and after solution annealing. Scanning TEM (STEM) is conducted to further analyze the inclusions, with the resulting images shown in Figure 11. Inclusions rich in Mn, Si, and O and in Mn and O are observed at a size of 20 nm in the as-built specimen (Figure 11a). These spherical particles are identified as $MnSiO_3$ and MnO inclusions. After solution annealing, the enriched elements are transformed into Mn, Cr, and O (Figure 11b–d), implying an inclusion transformation. Specifically, we observe signs of outward Si diffusion in HT-5. The spherical particles are identified as $MnCr_2O_4$ inclusions. With increasing solution annealing time, the size of the inclusions systematically increased from 20 nm in the HT-5 specimen to 50 nm in the HT-30 specimen and ultimately, to 100 nm in the HT-120 specimen.

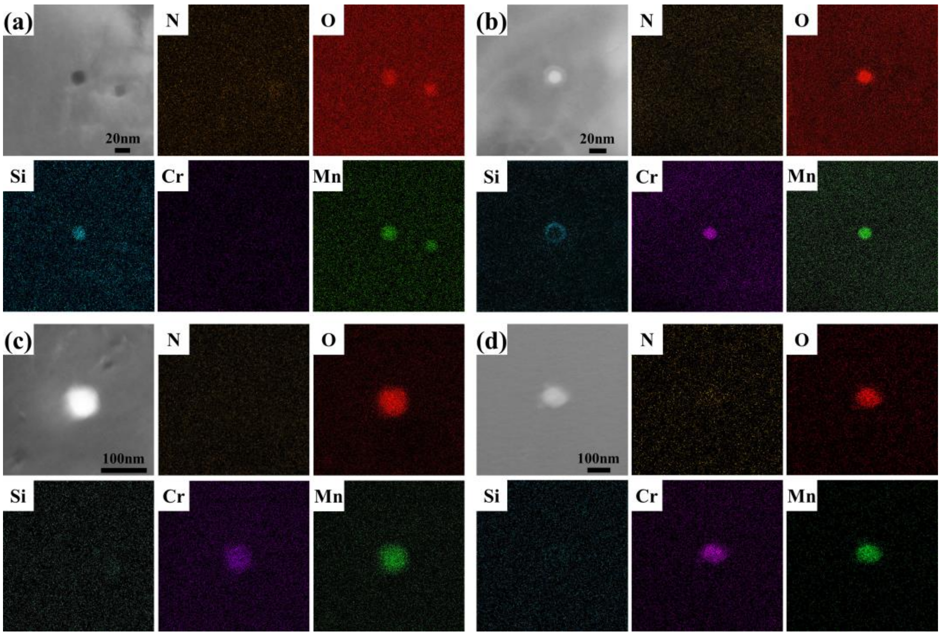

Figure 11. STEM-EDX mappings of inclusions, before and after solution annealing: (**a**) as-built, (**b**) HT-5, (**c**) HT-30, and (**d**) HT-120.

The as-built specimen, which is mostly ferrite, showed even distributions of Cr, Mn, Mo, and Ni (Figure 12a). After solution annealing, Mo, Mn, and Cr are partitioned into ferrite, and Ni into austenite (Figure 12b). MnO and $MnCr_2O_4$ appear only in the austenitic phase.

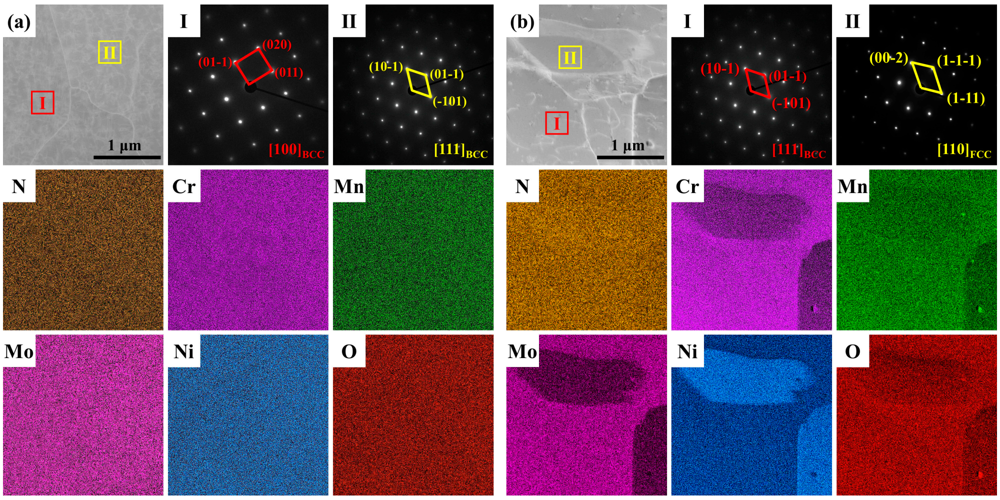

Figure 12. STEM-EDS maps showing partitioning of alloying elements between ferrite and austenite; inset I and inset II are the corresponding SAD patterns of the respective regions: (**a**) as-built, (**b**) HT-30.

3.2. Mechanical Properties

To illustrate the effect of solution annealing time on mechanical properties, the stress–strain responses of the various specimens are evaluated here (Figure 13), obtained by tensile testing, as described in Section 2.3. All specimens except for the as-built specimen demonstrate remarkable strength and plasticity. Figure 14a–c summarizes the key mechanical properties determined from the tensile test results. The as-built specimen, composed of an entirely ferritic microstructure, exhibits a significantly higher ultimate tensile strength (UTS) and yield strength (YS) than the annealed specimens, at 1078.8 MPa and 987.5 MPa, respectively. However, its maximum elongation is only 15.2%. Although solution annealing appears to have decreased the strength of the annealed specimens compared to that of the as-built specimen, it also increases their elongation. More specifically, increasing solution annealing time corresponds with decreasing UTS and YS. The elongation rate initially increases with annealing time, from 28.1% in the HT-5 specimen to 32.2% in the HT-30 specimen, but subsequently decreases to 28.9% in the HT-120 specimen. Figure 14d shows the UTS of the HT-30 specimen as a function of elongation. Compared with the existing literature and rolled samples, the HT-30 sample demonstrates exceptional strength–plasticity matching.

SEM images of the tensile fractures of the different specimens are presented in Figure 15. For the as-built specimen (Figure 15a), the fracture surface exhibits mixed characteristics, with smooth surfaces and small dimples. Therefore, it can be inferred that the fracture mechanism of the specimen is quasi-cleavage fracture, which is consistent with the high strength and low elongation observed in the tensile test. After solution annealing (Figure 15b–d), all the fracture surfaces are composed of smaller dimples, indicating ductile fracture. This corresponds with the higher elongation observed in these specimens after tensile deformation.

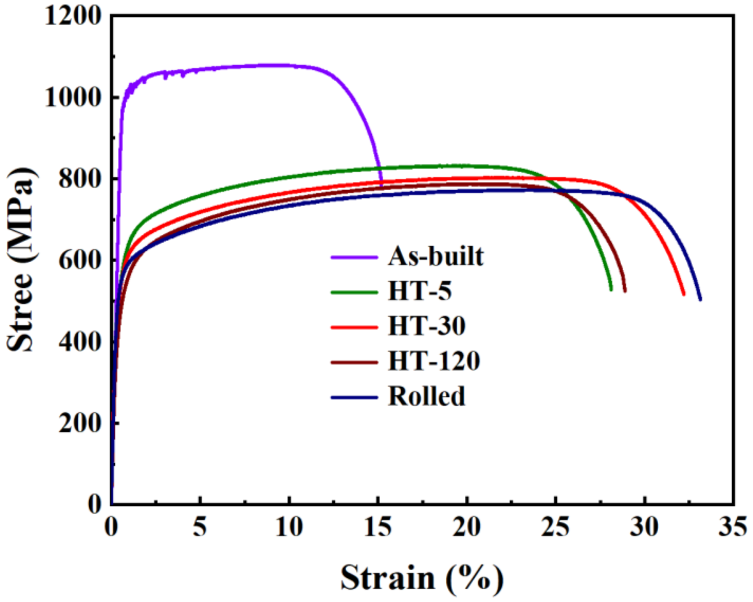

Figure 13. Stress–strain curves, before and after solution annealing.

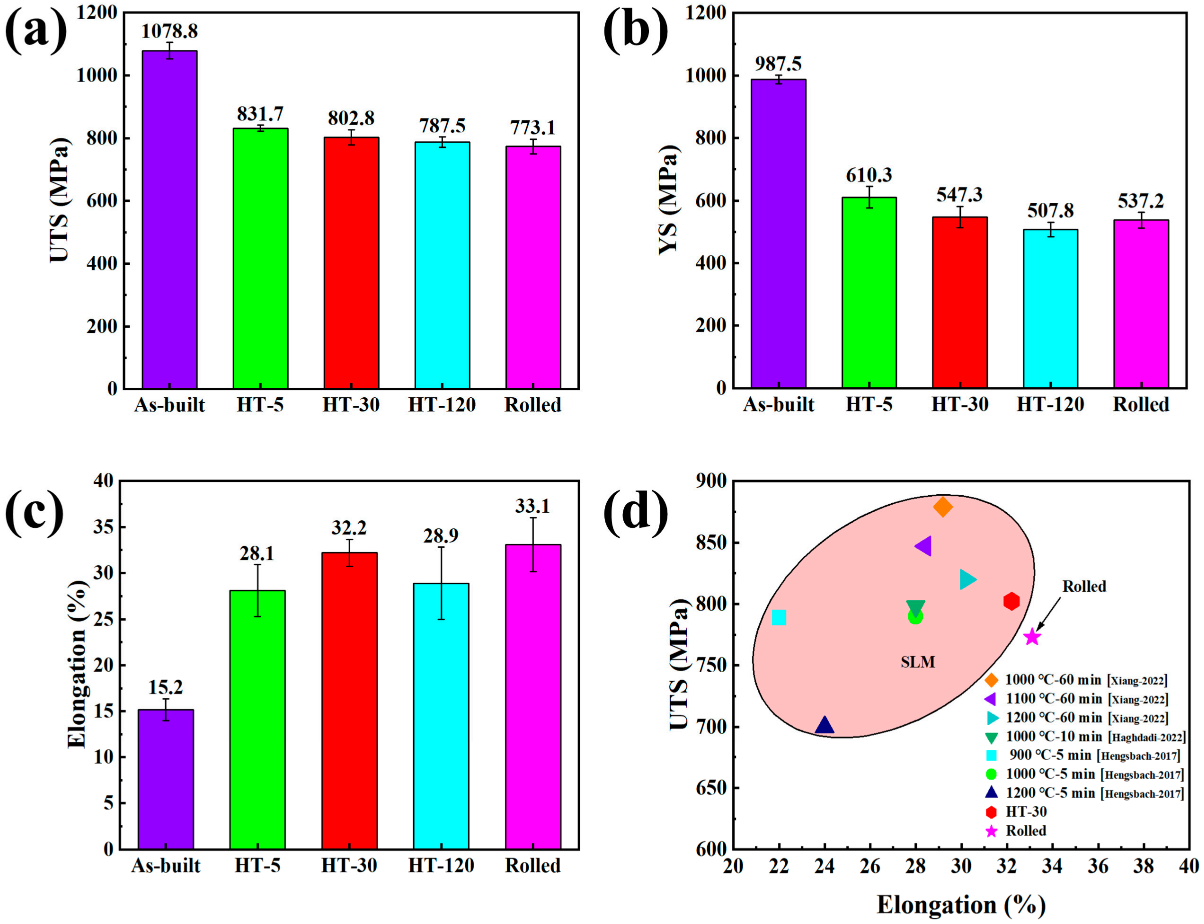

Figure 14. Results of mechanical property testing: (**a**) ultimate tensile strength (UTS), (**b**) yield strength (YS), (**c**) elongation, and (**d**) summary of UTS versus elongation for 2205 alloys [4,29,31].

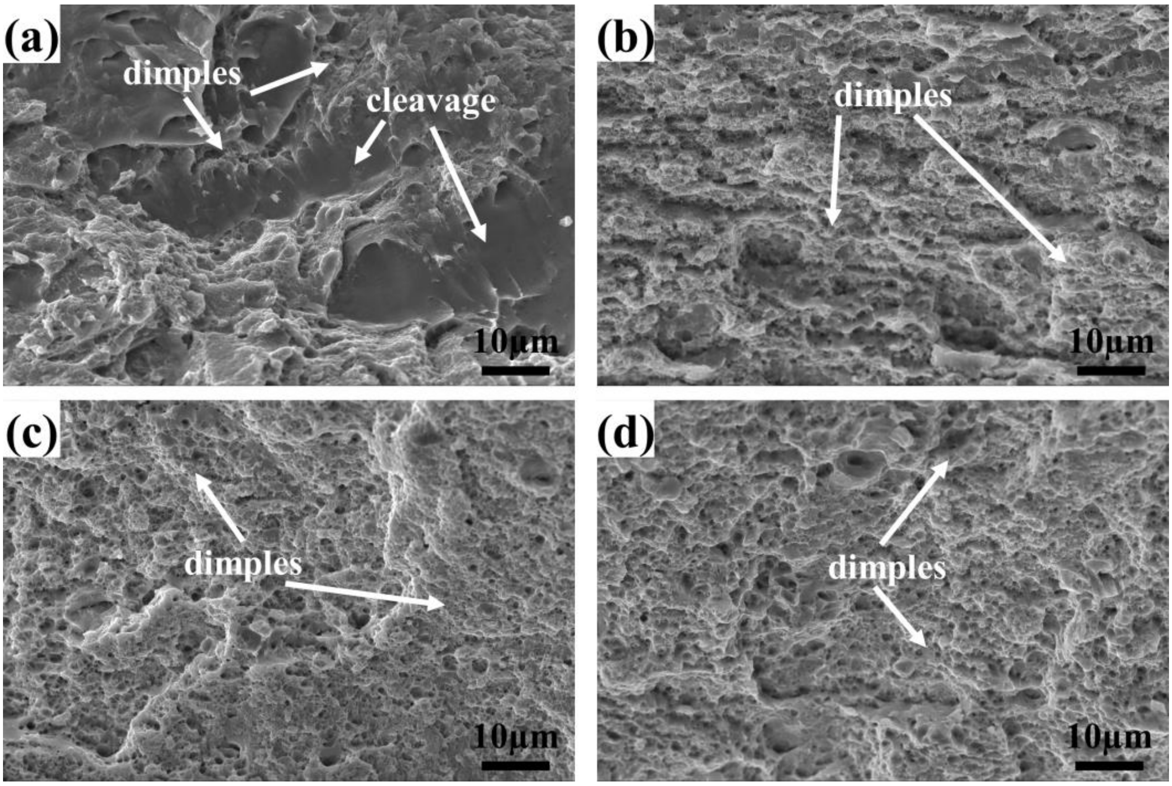

Figure 15. Specimen fracture surfaces: (**a**) as-built, (**b**) HT-5, (**c**) HT-30, and (**d**) HT-120.

4. Discussion

4.1. Formation and Evolution of Oxide Inclusions

The oxygen content in stainless steel produced by SLM is 4–6 times higher than that of cast, forged, and welded stainless steel. There are three main sources of oxygen [41]: (1) initial oxide inclusions and a surface oxide layer (approximately 3 nm thick) present in the raw powder material, (2) oxidation occurring on the melt pool surface during SLM, and (3) severe oxidation of the splattered particles that flow back into the melt pool. The powders used in SLM are typically produced through gas or water atomization processes, which significantly increase the likelihood of oxygen contamination in the initial powder. The oxygen content of gas-atomized steel powders is usually approximately 200 ppm [42], whereas that of water-atomized powders tends to be higher. During the laser scanning process, the internal and surface oxide inclusions in the powder are redissolved and nucleated to form nanoscale oxide inclusions, the chemical properties of which depend primarily on the oxygen-affinity elements in the alloy. In addition, even in the presence of argon gas in the build chamber during the SLM process, as in this study, a trace amount of oxygen (~0.02%) is likely to remain owing to the limitations of the equipment [43]. Hence, the melt pool surface may come into contact with residual oxygen, causing the enrichment of oxygen-affinity elements such as Mn, Si, and Cr, and leading to the formation of an oxide layer on the melt pool surface [44]. As the melt pool is vigorously agitated, the surface oxide layer fragments into multiple spherical oxide inclusions, which are subsequently retained in the stainless steel portion during solidification [45]. This melt pool splashing is a result of the combined effects of recoil pressure caused by metal vaporization, Marangoni convection, and thermal effects [43]. Although the lateral gas flow applied during the printing process helps blow most of the splattered particles off the powder surface, the airflow velocity should not be too high, as an excessive velocity may also blow away the newly deposited powder. Therefore, some small splattered particles inevitably mix with the unmelted powder and reflow into the melt pool.

Regarding the transformation of $MnSiO_3$ to $MnCr_2O_4$, the presence of residual Si, as shown in Figure 11b, suggests that $MnSiO_3$ may be a transient phase of $MnCr_2O_4$. $MnCr_2O_4$ is more thermodynamically stable than $MnSiO_3$ [46]; however, the metastable MnSiO3 is formed in the as-built specimens because of the extremely high cooling rate. After solution annealing, the increased chemical driving force promotes the diffusion of Si outwards and that of Cr towards the oxide particles, resulting in the transformation of metastable $MnSiO_3$ into stable $MnCr_2O_4$.

Predictably, the appearance of inclusions has a certain effect on the material microstructure and properties. In this study, the inclusions gradually coarsen with increasing solution annealing time (Figure 11), resulting in decreases in the UTS and YS (Figure 14). This aligns with the work of Yan et al. [46], who confirmed that the dispersion-strengthening effect of inclusions decreases with the coarsening of inclusions. The effect of inclusions on phase transformation is discussed further in Section 4.2.

4.2. Phase Transition

The EBSD results show that the ferrite content of the as-built specimen reached 99.9% (Figure 4a). To investigate why the SLM-manufactured 2205 DSS is predominantly composed of ferrite, Thermo-Calc 2023a software is used to predict the relevant phase diagrams (Figure 16a). During the initial solidification, 100% ferrite is formed in the simulation, which can be attributed to the higher content of ferrite-forming elements in DSS compared with that of austenite-forming elements. Additionally, 2205 DSS exhibits the F solidification mode, and the phase transformation sequence is $L \rightarrow L + \delta \rightarrow \delta \rightarrow \delta + \gamma$. The transformation of ferrite into austenite occurs only when the temperature is below the ferrite solubility line. However, owing to the extremely high cooling rate (10^5–10^6 K/S) during SLM processing [47], there is not sufficient time for the transformation of ferrite to austenite to occur. Another possible explanation is the loss of the stabilizing element N in austenite during SLM, as shown in Table 4. It is for these reasons that the as-built specimens are almost completely ferritic.

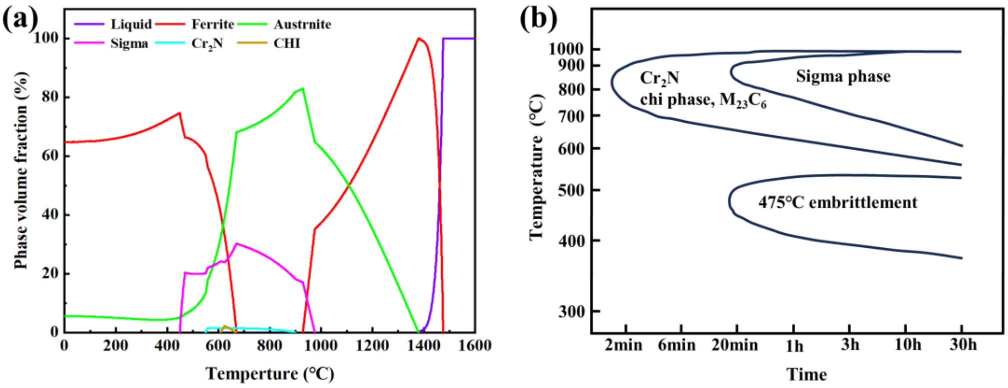

Figure 16. (**a**) Thermal equilibrium phase diagram of 2205 DSS calculated by Thermal-Calc. (**b**) Precipitation diagram of 2205 DSS [48].

Table 4. Nitrogen content in the 2205 DSS powder and as-built specimen.

	N wt/%
Powder	0.19
As-built	0.16

There is no precipitation of harmful phases during the solution annealing at 1000 °C (Figure 16b). The austenite formed during solid solution annealing differs from that formed after welding. Welding incurs two types of austenite formations: (1) the liquid phase first transforms into ferrite, and then the ferrite transforms into austenite through a solid-state phase transformation; or (2) the liquid phase transforms into ferrite because of the enrichment of Cr and Mo in ferrite and the depletion of Ni, Ni-rich regions are formed near the ferrite, and the residual liquid phase near these regions can directly solidify into austenite. Most of these austenite samples precipitate at the ferrite grain boundaries, and secondary austenite samples can also form after multipass welding.

However, because 1000 °C is below the material's liquidus temperature, the austenite formed after solid solution annealing at 1000 °C can only be formed through the solid-state phase transformation of ferrite, which resembles the "diffusion-limited" displacement mechanism [49]. Figure 17 shows a schematic of the ferrite-to-austenite transformation. The elemental distribution in the SLM-manufactured DSS is initially uniform, as in the as-built samples (Figure 17a). However, during solution annealing, enriched Ni and depleted Cr, Mo, and Mn regions form inside the ferrite (Figure 17b), the ferrite transforms into austenite in these regions, and the oxide inclusions provide nucleation sites for austenite formation. With increasing solution annealing time, these regions gradually increase in size, and the austenite and oxide inclusions also grow (Figure 17c). These austenites are randomly distributed inside the ferrite and are all primary austenites.

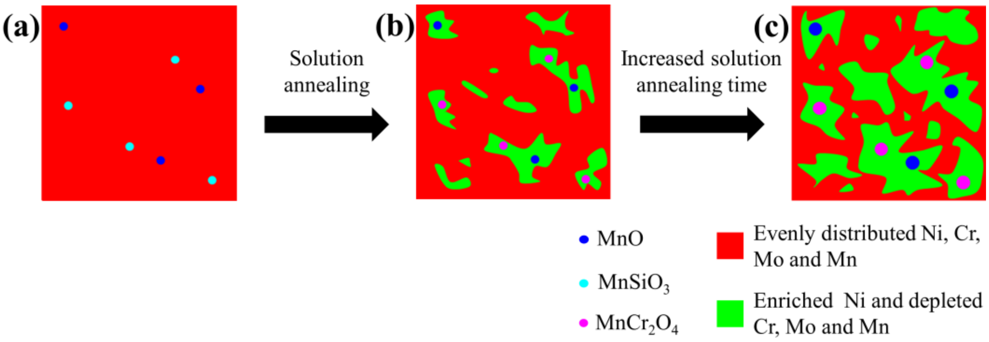

Figure 17. Schematic diagram of the solid-state phase transformation from ferrite to austenite: (**a**) as-built status, (**b**) after solution annealing, (**c**) after increased solution annealing time.

The ferrite in the as-built specimen is directly formed through solidification. Its grain morphology is determined by the ratio of the temperature gradient (G) to the growth rate (R) of the solid–liquid interface, known as G/R. Columnar grains are more likely to appear at higher G/R values [50]. During the solidification process, the grain growth rate R at the edge of the melt pool is slower than that at the center, whereas the temperature gradient G distribution is the opposite. A higher G/R value led to the growth of columnar grains along the direction perpendicular to the melt pool boundary, opposite to the direction of heat conduction, with the resulting columnar grains oriented along the <001> direction, as shown in Figure 5a.

The texture strength is reduced after solution annealing owing to phase transformation [51]. The phase transformation from BCC to FCC is similar to that of the Bain model for martensitic transformations [52]. During the phase transformation, the new austenite does not retain the original orientation of the ferrite, having a density of only 1/3 of that of the original ferrite orientation [53]. Therefore, this particular phase transformation not only weakens the texture strength generally but also leads to a relatively weaker texture strength of austenite compared to ferrite (Figure 5e–g). However, the textural strength of the HT-120 specimen is higher than that of the HT-30 specimen with the increased degree of phase transformation. This is because, with an increase in the solution annealing time, the grain sizes of austenite and ferrite increase (as shown in Table 3 for the HT-120 specimen), resulting in an increase in the texture strength. Hutchinson et al. [54] also observed texture-sharpening in ferrites after normal grain growth.

4.3. Evolution of Mechanical Properties

In tensile tests, the as-built SLM-manufactured DSS specimens exhibit high UTS but low elongation. This is explained by several factors. First, the ferritic phase is harder than the austenitic phase, and the microstructure of the as-built specimen is predominantly ferritic, making this phenomenon more pronounced. Additionally, high-density dislocations (evident in Figure 10a) severely reduce the dislocation slip pathways and impede dislocation motion. Furthermore, the dispersion-strengthening effect of the nanoscale oxide inclusions and the strong texture of the specimens in the <001> direction may also be influential factors.

After solution annealing, the strength of all specimens is lower compared to that of the as-built specimen, while the elongation increases significantly. This is mainly due to the significant increase in the austenite content (as shown in Figure 4). In addition, solution annealing greatly reduces dislocation density (Figure 10b), as well as the texture strength (during the phase transformation process). Crystal orientation relationships (K-S and Pitsch) are adopted between the parent and daughter phases (Figure 9), minimizing the interfacial energy of the nucleation and growth processes. This orientation relationship not only facilitates the propagation of dislocations from one phase to another but also reduces the distribution of residual stress [55]. Finally, the dynamic recrystallization process transforms the microstructure from columnar grains to equiaxed grains, resulting in a significant reduction in the grain size (Table 2), which leads to a more balanced mechanical performance.

The UTS and YS of the specimens gradually decreased with an increase in the solution annealing time, and this can be attributed to the coarsening of the grain size and the reduction in ferrite content. However, the elongation rate demonstrates a different trend, i.e., initially increasing and then decreasing with annealing time. The initial increase is explained by the same factors as the decreased strength after solution annealing. The focus now is on explaining the subsequent decrease in elongation.

First, the main explanation behind this is the coarsening of the grain size in the HT-120 specimen, which causes an increase in the texture strength, as mentioned in Section 4.2. Additionally, the number of HAGBs in the HT-120 specimen is significantly lower than that in the HT-30 specimen (Figure 8). In general, the plasticity level of a material can be understood as the amount of energy absorbed by the material during deformation and fracture. The energy absorbed by the material is manifested at the microstructural level as the formation of defects or the dissipation of energy due to their movement. Grain boundaries, as planar defects, play an important role in this process by coordinating adjacent grains, hindering defect motion, and altering crack propagation paths. Compared with LAGBs, HAGBs exhibit irregular atomic arrangements, making crack propagation more difficult. The plasticity (and hence elongation) of HT-120 is thus lower than that of HT-30.

5. Conclusions

The 2205 DSS specimens are successfully prepared by SLM, and their microstructure and mechanical properties before and after solution annealing are studied. The following conclusions are obtained:

1. The as-built (un-annealed) specimen exhibits a high strength (UTS = 1078.8 MPa) and low elongation (15.2%). This is attributed to its predominantly ferritic microstructure, high-density dislocations, and strong {001} texture.
2. Solid-solution treatment can restore the dual-phase microstructure, reduce the dislocation density, weaken the texture, and decrease the grain size of DSS, leading to a significant improvement in the elongation of the annealed samples and a corresponding decrease in strength. The UTS and YS of the HT-30 specimen are measured as 802.8 MPa and 547.3 MPa, respectively, with an elongation of 32.2%. Except for their elongation, the mechanical properties of the annealed DSS specimens are generally superior to those of the rolled specimens.

3. Extending the solution annealing time increases the extent of transformation from ferrite to austenite, thereby reducing the texture strength. However, if the time is further increased, the grain size will also increase, leading to an increase in texture strength. Additionally, the nucleation of austenite on the surface of ferrite always results inLAGBs, which leads to a reduction in HAGBs. These factors contribute to a nonlinear change in elongation in response to solution annealing time.
4. During solution annealing, enriched Ni and depleted Cr, Mo, and Mn regions form inside the ferrite, and the ferrite in these regions is transformed into austenite. Simultaneously, the transformation of $MnSiO_3$ into $CrMnO_4$ provides nucleation sites for austenite formation. Together, these result in the recovery of the dual-phase microstructure of DSS.

Author Contributions: Conceptualization, H.L. and J.M.; methodology, Y.S.; writing—original draft preparation, H.L. and X.B.; writing—review and editing, H.L. and J.M.; supervision, G.L. and W.Z.; funding acquisition, Y.S. All authors have read and agreed to the published version of the manuscript.

Funding: This work was supported by the central government guides' local science and technology projects (grant No. 23ZYQA308); the Key Project of Research and Innovation in Universities (grant No. 2024CXPT-06); the Scientific and Technological Projects of Jiayuguan (grant No. 23-15); the Project of the National Natural Science Foundation of China [grant number 51961022]; and the Excellent Doctor Program in Gansu Province, supported by the Gansu Provincial Science and Technology Plan (No. 22JRRA793).

Data Availability Statement: The data are contained within the article.

Conflicts of Interest: The authors declare no conflicts of interest.

References

1. Zhang, Y.; Wang, C.; Reddy, K.M.; Li, W.; Wang, X. Study on the deformation mechanism of a high-nitrogen duplex stainless steel with excellent mechanical properties originated from bimodal grain design. *Acta Mater.* **2022**, *226*, 117670. [CrossRef]
2. Chen, Y.; Yang, B.; Zhou, Y.; Wu, Y.; Zhu, H. Evaluation of pitting corrosion in duplex stainless steel $Fe_{20}Cr_9Ni$ for nuclear power application. *Acta Mater.* **2020**, *197*, 172–183. [CrossRef]
3. Zhang, D.; Liu, A.; Yin, B.; Wen, P. Additive manufacturing of duplex stainless steels—A critical review. *J. Manuf. Process.* **2022**, *73*, 496–517. [CrossRef]
4. Xiang, H.; Zhao, W.; Lu, Y. Effect of solution temperature on microstructure and mechanical properties of selective laser melted Fe-22Cr-5Ni-0.26N duplex stainless steel. *J. Mater. Res. Technol. JMR&T* **2022**, *19*, 1379–1389. [CrossRef]
5. Azami, M.; Siahsarani, A.; Hadian, A.; Kazemi, Z.; Rahmatabadi, D.; Kashani-Bozorg, S.F.; Abrinia, K. Laser powder bed fusion of Alumina/Fe-Ni ceramic matrix particulate composites impregnated with a polymeric resin. *J. Mater. Res. Technol. JMR&T* **2023**, *24*, 3133–3144. [CrossRef]
6. Lewandowski, J.J.; Seifi, M. Metal Additive Manufacturing: A Review of Mechanical Properties. In *Annual Review of Materials Research*; Clarke, D.R., Ed.; Annual Review: San Mateo, CA, USA, 2016; Volume 46, pp. 151–186.
7. Olakanmi, E.O.; Cochrane, R.F.; Dalgarno, K.W. A review on selective laser sintering/melting (SLS/SLM) of aluminium alloy powders: Processing, microstructure, and properties. *Prog. Mater. Sci.* **2015**, *74*, 401–477. [CrossRef]
8. Lenders, S.; Thone, M.; Riemer, A.; Niendorf, T.; Troster, T.; Richard, H.A.; Maier, H.J. On the mechanical behaviour of titanium alloy $TiAl_6V_4$ manufactured by selective laser melting: Fatigue resistance and crack growth performance. *Int. J. Fatigue* **2013**, *48*, 300–307. [CrossRef]
9. Song, B.; Dong, S.; Zhang, B.; Liao, H.; Coddet, C. Effects of processing parameters on microstructure and mechanical property of selective laser melted Ti_6Al_4V. *Mater. Des.* **2012**, *35*, 120–125. [CrossRef]
10. Kimura, T.; Nakamoto, T. Microstructures and mechanical properties of A356 ($AlSi_7Mg_{0.3}$) aluminum alloy fabricated by selective laser melting. *Mater. Des.* **2016**, *89*, 1294–1301. [CrossRef]
11. Rao, H.; Giet, S.; Yang, K.; Wu, X.; Davies, C.H.J. The influence of processing parameters on aluminium alloy A357 manufactured by Selective Laser Melting. *Mater. Des.* **2016**, *109*, 334–346. [CrossRef]
12. Popovich, A.; Sufiiarov, V.; Polozov, I.; Borisov, E.; Masaylo, D.; Orlov, A. Microstructure and mechanical properties of additive manufactured copper alloy. *Mater. Lett.* **2016**, *179*, 38–41. [CrossRef]
13. Scudino, S.; Unterdoerfer, C.; Prashanth, K.G.; Attar, H.; Ellendt, N.; Uhlenwinkel, V.; Eckert, J. Additive manufacturing of Cu-10Sn bronze. *Mater. Lett.* **2015**, *156*, 202–204. [CrossRef]
14. Aydinoez, M.E.; Brenne, F.; Schaper, M.; Schaak, C.; Tillmann, W.; Nellesen, J.; Niendorf, T. On the microstructural and mechanical properties of post-treated additively manufactured Inconel 718 superalloy under quasi-static and cyclic loading. *Mater. Sci. Eng. A Struct. Mater. Prop. Microstruct. Process.* **2016**, *669*, 246–258. [CrossRef]

15. Kanagarajah, P.; Brenne, F.; Niendorf, T.; Maier, H.J. Inconel 939 processed by selective laser melting: Effect of microstructure and temperature on the mechanical properties under static and cyclic loading. *Mater. Sci. Eng. A Struct. Mater. Prop. Microstruct. Process.* **2013**, *588*, 188–195. [CrossRef]
16. Tillmann, W.; Schaak, C.; Nellesen, J.; Schaper, M.; Aydinoez, M.E.; Hoyer, K.P. Hot isostatic pressing of IN718 components manufactured by selective laser melting. *Addit. Manuf.* **2017**, *13*, 93–102. [CrossRef]
17. Brif, Y.; Thomas, M.; Todd, I. The use of high-entropy alloys in additive manufacturing. *Scr. Mater.* **2015**, *99*, 93–96. [CrossRef]
18. Niendorf, T.; Brenne, F.; Krooss, P.; Vollmer, M.; Gunther, J.; Schwarze, D.; Biermann, H. Microstructural Evolution and Functional Properties of Fe-Mn-Al-Ni Shape Memory Alloy Processed by Selective Laser Melting. *Metall. Mater. Trans. A Phys. Metall. Mater. Sci.* **2016**, *47*, 2569–2573. [CrossRef]
19. Fergani, O.; Wold, A.B.; Berto, F.; Brotan, V.; Bambach, M. Study of the effect of heat treatment on fatigue crack growth behaviour of 316L stainless steel produced by selective laser melting. *Fatigue Fract. Eng. Mater. Struct.* **2018**, *41*, 1102–1119. [CrossRef]
20. Guan, K.; Wang, Z.; Gao, M.; Li, X.; Zeng, X. Effects of processing parameters on tensile properties of selective laser melted 304 stainless steel. *Mater. Des.* **2013**, *50*, 581–586. [CrossRef]
21. Peng, T.; Chen, C. Influence of Energy Density on Energy Demand and Porosity of 316L Stainless Steel Fabricated by Selective Laser Melting. *Int. J. Precis. Eng. Manuf. Green Technol.* **2018**, *5*, 55–62. [CrossRef]
22. Fang, R.; Deng, N.; Zhang, H.; Wang, G.; Su, Y.; Zhou, H.; Gao, K.; Gu, L. Effect of selective laser melting process parameters on the microstructure and properties of a precipitation hardening stainless steel. *Mater. Des.* **2021**, *212*, 110265. [CrossRef]
23. Kudzal, A.; McWilliams, B.; Hofmeister, C.; Kellogg, F.; Yu, J.; Taggart-Scarff, J.; Liang, J. Effect of scan pattern on the microstructure and mechanical properties of Powder Bed Fusion additive manufactured 17-4 stainless steel. *Mater. Des.* **2017**, *133*, 205–215. [CrossRef]
24. Stashkov, A.; Schapova, E.; Tsar'kova, T.; Sazhina, E.; Bychenok, V.; Fedorov, A.; Kaigorodov, A.; Ezhov, I. Magnetic, electric properties and hardness of 17-4 PH stainless steel fabricated by selective laser melting. *J. Phys. Conf. Ser.* **2019**, *1389*, 012124. [CrossRef]
25. Nigon, G.N.; Isgor, O.B.; Pasebani, S. The effect of annealing on the selective laser melting of 2205 duplex stainless steel: Microstructure, grain orientation, and manufacturing challenges. *Opt. Laser Technol.* **2021**, *134*, 106643. [CrossRef]
26. Saeidi, K.; Kevetkova, L.; Lofaj, F.; Shen, Z. Novel ferritic stainless steel formed by laser melting from duplex stainless steel powder with advanced mechanical properties and high ductility. *Mater. Sci. Eng. A Struct. Mater. Prop. Microstruct. Process.* **2016**, *665*, 59–65. [CrossRef]
27. Chen, Y.H.; Sun, S.W.; Zhang, T.M.; Zhou, X.W.; Li, S.H. Effects of post-weld heat treatment on the microstructure and mechanical properties of laser-welded NiTi/304SS joint with Ni filler. *Mater. Sci. Eng. A Struct. Mater. Prop. Microstruct. Process.* **2020**, *771*, 138545. [CrossRef]
28. Jiang, Y.L.; Fang, J.X.; Ma, G.Z.; Tian, H.L.; Zhang, D.B.; Cao, Y. Microstructure and properties of an as-deposited and post treated high strength carbide-free bainite steel fabricated via laser powder deposition. *Mater. Sci. Eng. A Struct. Mater. Prop. Microstruct. Process.* **2021**, *824*, 141791. [CrossRef]
29. Hengsbach, F.; Koppa, P.; Duschik, K.; Holzweissig, M.J.; Burns, M.; Nellesen, J.; Tillmann, W.; Troester, T.; Hoyer, K.-P.; Schaper, M. Duplex stainless steel fabricated by selective laser melting—Microstructural and mechanical properties. *Mater. Des.* **2017**, *133*, 136–142. [CrossRef]
30. Pan, M.; Zhang, X.; Chen, P.; Su, X.; Misra, R.D.K. The effect of chemical composition and annealing condition on the microstructure and tensile properties of a resource-saving duplex stainless steel. *Mater. Sci. Eng. A Struct. Mater. Prop. Microstruct. Process.* **2020**, *788*, 139540. [CrossRef]
31. Haghdadi, N.; Ledermueller, C.; Chen, H.; Chen, Z.; Liu, Q.; Li, X.; Rohrer, G.; Liao, X.; Ringer, S.; Primig, S. Evolution of microstructure and mechanical properties in 2205 duplex stainless steels during additive manufacturing and heat treatment. *Mater. Sci. Eng. A Struct. Mater. Prop. Microstruct. Process.* **2022**, *835*, 142695. [CrossRef]
32. Papula, S.; Song, M.; Pateras, A.; Chen, X.-B.; Brandt, M.; Easton, M.; Yagodzinskyy, Y.; Virkkunen, I.; Haenninen, H. Selective Laser Melting of Duplex Stainless Steel 2205: Effect of Post-Processing Heat Treatment on Microstructure, Mechanical Properties, and Corrosion Resistance. *Materials* **2019**, *12*, 2468. [CrossRef]
33. Aegerter, J.; Kühn, H.-J.; Frenz, H.; Weißmüller, C. EN ISO 6892-1:2009 Tensile Testing: Initial Experience from the Practical Implementation of the New Standard*. *Materialprufung* **2011**, *53*, 595–603. [CrossRef]
34. Salvetr, P.; Školáková, A.; Melzer, D.; Brázda, M.; Duchoň, J.; Drahokoupil, J.; Svora, P.; Msallamová, Š.; Novák, P. Characterization of super duplex stainless steel SAF2507 deposited by directed energy deposition. *Mater. Sci. Eng. A* **2022**, *857*, 144084. [CrossRef]
35. Freitas, B.J.M.; Rodrigues, L.C.M.; Claros, C.A.E.; Botta, W.J.; Koga, G.Y.; Bolfarini, C. Ferritic-induced high-alloyed stainless steel produced by laser powder bed fusion (L-PBF) of 2205 duplex stainless steel: Role of microstructure, corrosion, and wear resistance. *J. Alloys Compd.* **2022**, *918*, 13. [CrossRef]
36. Ciftci, N.; Ellendt, N.; Coulthard, G.; Barreto, E.S.; Mädler, L.; Uhlenwinkel, V. Novel Cooling Rate Correlations in Molten Metal Gas Atomization. *Metall. Mater. Trans. B Proc. Metall. Mater. Proc. Sci.* **2019**, *50*, 666–677. [CrossRef]
37. Haghdadi, N.; Cizek, P.; Hodgson, P.D.; He, Y.; Sun, B.; Jonas, J.J.; Rohrer, G.S.; Beladi, H. New insights into the interface characteristics of a duplex stainless steel subjected to accelerated ferrite-to-austenite transformation. *J. Mater. Sci.* **2020**, *55*, 5322–5339. [CrossRef]

38. Dandekar, T.R.; Kumar, A.; Khatirkar, R.K.; Kumar, D.; Suwas, S. Effect of microstructure and texture on the evolution of mechanical properties in a cold rolled and annealed UNS S32101 lean duplex stainless steel sheet. *Mater. Chem. Phys.* **2023**, *299*, 127485. [CrossRef]
39. Kumar, A.; Khatirkar, R.K.; Chalapathi, D.; Kumar, G.; Suwas, S. Microstructure and Texture Development during Cold Rolling in UNS S32205 and UNS S32760 Duplex Stainless Steels. *Metall. Mater. Trans. A Phys. Metall. Mater. Sci.* **2017**, *48*, 2349–2362. [CrossRef]
40. Oku, N.; Asakura, K.; Inoue, J.; Koseki, T. In-situ Observation of Phase Transformation in Steels. In Proceedings of the 8th International Conference on Trends in Welding Research, Pine Mountain, GA, USA, 1–6 June 2008; pp. 272–276.
41. Deng, P.; Karadge, M.; Rebak, R.B.; Gupta, V.K.; Prorok, B.C.; Lou, X.Y. The origin and formation of oxygen inclusions in austenitic stainless steels manufactured by laser powder bed fusion. *Addit. Manuf.* **2020**, *35*, 101334. [CrossRef]
42. Klar, E.; Samal, P.K. *Powder Metallurgy Stainless Steels: Processing, Microstructures, and Properties*; ASM International: Detroit, MI, USA, 2007.
43. Wang, D.; Wu, S.B.; Fu, F.; Mai, S.Z.; Yang, Y.Q.; Liu, Y.; Song, C.H. Mechanisms and characteristics of spatter generation in SLM processing and its effect on the properties. *Mater. Des.* **2017**, *117*, 121–130. [CrossRef]
44. Simonelli, M.; Tuck, C.; Aboulkhair, N.T.; Maskery, I.; Ashcroft, I.; Wildman, R.D.; Hague, R. A Study on the Laser Spatter and the Oxidation Reactions During Selective Laser Melting of 316L Stainless Steel, Al-Si10-Mg, and Ti-6Al-4V. *Metall. Mater. Trans. A Phys. Metall. Mater. Sci.* **2015**, *46*, 3842–3851. [CrossRef]
45. Boegelein, T.; Dryepondt, S.N.; Pandey, A.; Dawson, K.; Tatlock, G.J. Mechanical response and deformation mechanisms of ferritic oxide dispersion strengthened steel structures produced by selective laser melting. *Acta Mater.* **2015**, *87*, 201–215. [CrossRef]
46. Yan, F.Y.; Xiong, W.; Faierson, E.; Olson, G.B. Characterization of nano-scale oxides in austenitic stainless steel processed by powder bed fusion. *Scr. Mater.* **2018**, *155*, 104–108. [CrossRef]
47. DebRoy, T.; Wei, H.L.; Zuback, J.S.; Mukherjee, T.; Elmer, J.W.; Milewski, J.O.; Beese, A.M.; Wilson-Heid, A.; De, A.; Zhang, W. Additive manufacturing of metallic components—Process, structure and properties. *Prog. Mater. Sci.* **2018**, *92*, 112–224. [CrossRef]
48. Zucato, I.; Moreira, M.C.; Machado, I.F.; Lebrão, S.M.G. Microstructural Characterization and the Effect of Phase Transformations on Toughness of the UNS S31803 Duplex Stainless Steel Aged Treated at 850 °C. *Mater. Res.* **2002**, *5*, 385–389. [CrossRef]
49. Christian, J.W. Crystallographic theories, interface structures, and transformation mechanisms. *Metall. Mater. Trans. A* **1994**, *25*, 1821–1839. [CrossRef]
50. Wei, H.L.; Mukherjee, T.; Zhang, W.; Zuback, J.S.; Knapp, G.L.; De, A.; DebRoy, T. Mechanistic models for additive manufacturing of metallic components. *Prog. Mater. Sci.* **2021**, *116*, 113. [CrossRef]
51. Ghaffari, M.; Vahedi Nemani, A.; Nasiri, A. Microstructure and mechanical behavior of PH 13–8Mo martensitic stainless steel fabricated by wire arc additive manufacturing. *Addit. Manuf.* **2022**, *49*, 102374. [CrossRef]
52. Wang, K.; Shang, S.L.; Wang, Y.; Liu, Z.K.; Liu, F. Martensitic transition in Fe via Bain path at finite temperatures: A comprehensive first-principles study. *Acta Mater.* **2018**, *147*, 261–276. [CrossRef]
53. Du, C.C.; Ren, X.D.; Pan, Q.H.; Li, Y.J. Preferential orientation and mechanical properties anisotropy of wire and arc additive manufactured duplex stainless steel. *Mater. Charact.* **2022**, *194*, 112277. [CrossRef]
54. Hutchinson, B.; Ryde, L.; Bate, P. Transformation textures in steels. In *Icotom 14: Textures of Materials, Pts 1and 2*; Houtte, P.V., Kestens, L., Eds.; Trans Tech Publications Ltd.: Zurich, Switzerland, 2005; Volume 495–497, pp. 1141–1149.
55. Chalapathi, D.; Sivaprasad, P.V.; Kanjarla, A.K. A crystal plasticity investigation on the influence of orientation relationships on texture evolution during rolling in fcc/bcc two phase materials. *Mater. Today Commun.* **2022**, *31*, 103300. [CrossRef]